Received: 20 December 2019 | Revised: 18 March 2020 | Accepted: 10 May 2020

DOI: 10.1002/jnm.2776

SPECIAL ISSUE PAPER

WILEY

Conformally mapped polynomial chaos expansions for Maxwell's source problem with random input data

Niklas Georg[1,2] | **Ulrich Römer**[1]

[1]Department of Mechanical Engineering, Institut für Dynamik und Schwingungen (IDS), Technische Universität Braunschweig, Braunschweig, Germany

[2]Department of Electrical Engineering and Information Technology, Centre for Computational Engineering (CCE) and Institute for Accelerator Science and Electromagnetic Fields (TEMF), Technische Universität Darmstadt, Darmstadt, Germany

Correspondence
Niklas Georg, Department of Mechanical Engineering, Institut für Dynamik und Schwingungen (IDS), Technische Universität Braunschweig, Schleinitzstraße 20, 38106 Braunschweig, Germany.
Email: n.georg@tu-braunschweig.de

Funding information
Deutsche Forschungsgemeinschaft:, Grant/Award Numbers: RO4937/1-1, GSC 233

Abstract

Generalized Polynomial Chaos (gPC) expansions are well established for forward uncertainty propagation in many application areas. Although the associated computational effort may be reduced in comparison to Monte Carlo techniques, for instance, further convergence acceleration may be important to tackle problems with high parametric sensitivities. In this work, we propose the use of conformal maps to construct a transformed gPC basis, in order to enhance the convergence order. The proposed basis still features orthogonality properties and hence, facilitates the computation of many statistical quantities such as sensitivities and moments. The corresponding surrogate models are computed by pseudo-spectral projection using mapped quadrature rules, which leads to an improved cost accuracy ratio. We apply the methodology to Maxwell's source problem with random input data. In particular, numerical results for a parametric finite element model of an optical grating coupler are given.

KEYWORDS

conformal maps, nanoplasmonics, polynomial chaos, surrogate modeling, uncertainty quantification

1 | INTRODUCTION

Due to recent developments in uncertainty quantification (UQ),[1] studying random parameter variations within the numerical simulation of fields and waves comes into reach. The present study is motivated from the design of optical components and plasmonic structures, where relatively large variabilities of nano-scale geometrical parameters can be observed, see, for example, Ref.[2] In this work, we focus on the forward problem, that is, the propagation of uncertainties from the model inputs to the outputs, in order to compute moments and sensitivities for physical quantities of interest (QoIs). We rely on surrogate modeling[3] to reduce the computational complexity of sampling the underlying finite element (FE) Maxwell solver. Although motivated from a forward model perspective, the surrogate construction could equally be used in an inverse problem context. Examples of surrogate modeling in electromagnetics can be found for instance in Refs.,[4-6] where microwave circuits and accelerator cavities are considered.

Generalized polynomial chaos (gPC) expansions[7] are powerful tools for forward uncertainty propagation. They are based on an orthogonal polynomial basis with respect to the underlying probability distribution of the input parameters, to achieve good convergence properties. However, applying gPC may still be challenging, the computational cost

to handle large parameter uncertainties and parametric sensitivities for instance may be quite high. To remedy this issue, conformal maps can be utilized in order to improve the convergence of polynomial-based methods. The acceleration of quadrature methods by the use of conformal maps has been considered in Refs.[8-10] In Ref.,[11] conformal maps were combined with a stochastic collocation method, indicating significant gains in the accuracy of the corresponding surrogate model. In this work, we propose a new orthogonal basis by combining gPC and conformal maps. We note that, the proposed basis is constructed such that it fulfills the same orthogonality properties as gPC. Accordingly, advantages of gPC methods are preserved, for example, stochastic moments and Sobol coefficients can be directly computed from the expansion coefficients. It should also be noted that various approaches employing Polynomial Chaos expansions with basis rotation have been reported recently, see Refs.[12,13] Although, these works equally rely on mapped Polynomial Chaos approximations, the transformations are linear (affine) and not based on conformal mappings. Also, the emphasis there is on high dimensional approximation instead of convergence acceleration.

The proposed numerical scheme is applied to quantify uncertainties via surrogate models for Maxwell's equations in the frequency domain. In particular, we consider the source problem on periodic domains with a plane wave excitation and uncertainties in the material interface geometry. Such model equations can describe, for instance, the coupling into metal-insulator-metal (MIM) plasmon modes with subwavelength diffraction gratings,[2] which is illustrated in Figure 1A. Although illustrated by means of this particular application example, we note that the employed UQ methodologies apply in a much broader context.

This paper is structured as follows: Section 2 contains a brief description of Maxwell's source problem. The uncertainty quantification part can be found in Section 3, where we briefly recall standard gPC before discussing the proposed extension based on conformal mappings. Section 4 reports numerical results for an analytical RLC circuit and the aforementioned optical grating coupler, before conclusions are drawn.

2 | MAXWELL'S SOURCE PROBLEM

We consider Maxwell's source problem for periodic structures excited by an incident plane wave. For further details on this subject, we refer to Refs.[11,14] We start with the time-harmonic curl-curl equation

$$\nabla \times \left(\mu_{\mathrm{r}}^{-1} \nabla \times \mathbf{E}\right) - \omega^2 \varepsilon \mu_0 \mathbf{E} = 0 \quad \text{in } D, \tag{1}$$

for the electric field phasor $\mathbf{E}$ in the computational domain D, where ω denotes the angular frequency, ε the complex permittivity and μ_{r}, μ_0 denote the relative and vacuum permeability, respectively. Note that Equation (1) assumes absence of charges and source currents in D. Based on Floquet's theorem (Ref.,[14] chapter 13), the computational domain D can be reduced to a unit cell of the periodic structure, as we assume a periodic excitation. Such a unit cell is depicted in Figure 1B. Due to the oblique angle of the incident wave, the excitation has a different periodicity than the geometry and, hence, periodic phase-shift boundary conditions need to be imposed on the respective boundaries. To truncate the structure in the non-periodic direction, a Floquet absorbing boundary condition and a perfect electric conductor (PEC) boundary condition are applied. This leads to the boundary value problem

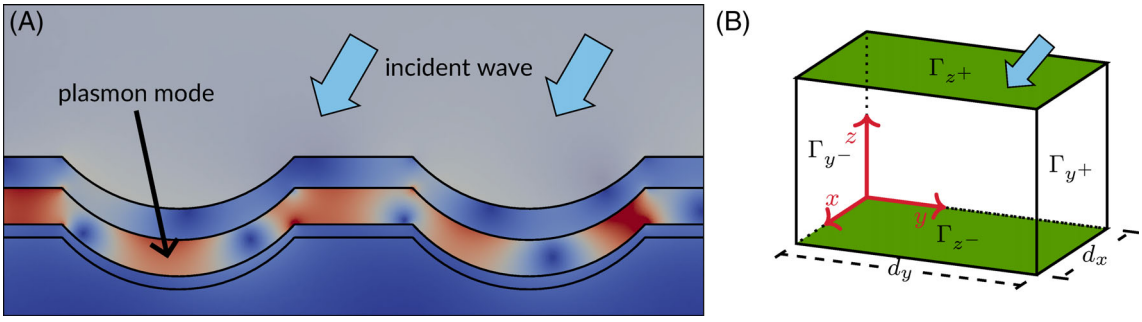

FIGURE 1 Scattering of periodic structure excited by an incident plane wave; illustrations based on Ref.[11]. A, Optical coupling into metal-insulator-metal (MIM) plasmon modes.[2] B, Sketch of considered unit cell corresponding to the computational domain D. The blue arrow illustrates the incident wavevector $\mathbf{k}^{\mathrm{inc}}$

$$\nabla \times \left(\mu_{\mathrm{r}}^{-1} \nabla \times \mathbf{E}\right) - \omega^2 \varepsilon \mu_0 \mathbf{E} = 0 \qquad \text{in } D \tag{2}$$

$$\mathbf{E}\Big|_{\Gamma_{x^+}} e^{jk_x^{\mathrm{inc}} d_x} = \mathbf{E}\Big|_{\Gamma_{x^-}} \qquad \text{on } \Gamma_{x^+} \cup \Gamma_{x^-} \tag{3}$$

$$\mathbf{E}\Big|_{\Gamma_{y^+}} e^{jk_y^{\mathrm{inc}} d_y} = \mathbf{E}\Big|_{\Gamma_{y^-}} \qquad \text{on } \Gamma_{y^+} \cup \Gamma_{y^-} \tag{4}$$

$$\mathbf{n} \times \mathbf{E} = 0 \qquad \text{on } \Gamma_{z^-} \tag{5}$$

$$\left(\mu_{\mathrm{r}}^{-1} \nabla \times \mathbf{E}\right) \times \mathbf{n} + \mathcal{F}(\mathbf{E}) = \mathcal{G}\left(\mathbf{E}^{\mathrm{inc}}\right) \qquad \text{on } \Gamma_{z^+}, \tag{6}$$

where we refer to (Ref.,[11] appendix A) for a derivation and definition of the functionals $\mathcal{F}(\cdot)$, $\mathcal{G}(\cdot)$.

We assume in the following that the complex permittivity ε depends smoothly on a parameter vector $\mathbf{y} \in \Xi \subset \mathbb{R}^N$. These parameters can then be used to model variations in the refractive indices or extinction coefficients of the (different) materials in D, as well as changes in the geometry of the material interfaces inside the domain D. Following a standard Galerkin procedure, cf. Ref.,[11] we then obtain a FE model in the form

$$\text{find } \mathbf{e}(\mathbf{y}) \in V \text{ s.t.} \quad a_{\mathbf{y}}(\mathbf{e}(\mathbf{y}), \mathbf{v}) = l_{\mathbf{y}}(\mathbf{v}) \quad \forall \mathbf{v} \in V, \tag{7}$$

where $a_{\mathbf{y}}(\cdot,\cdot)$ is a continuous sesquilinear form, $l_{\mathbf{y}}(\cdot)$ is a continuous (anti)linear form and V denotes a discrete subspace of $\mathbf{H}(\mathrm{curl}; D)$,[15] enforcing periodic phase-shift conditions on the traces at the periodic boundaries and homogeneous Dirichlet conditions at Γ_{z^-}. To achieve a curl-conforming discretization of Equation (7), we employ Nédélec's elements of the first kind[16] and second order on a tetrahedral mesh of D. As QoI we consider the fundamental reflection coefficient $\mathcal{Q}(\mathbf{e}(\mathbf{y}))$, that is, a scattering parameter, which can be computed as an affine-linear functional of the electric field $\mathbf{e}$ in post-processing.[11] For brevity, we replace $\mathcal{Q}(\mathbf{e}(\mathbf{y}))$ by $\mathcal{Q}(\mathbf{y})$ in the following.

3 | UNCERTAINTY QUANTIFICATION

To account for uncertainty, we model the input parameters $\mathbf{y}$ as independent random variable (RVs) with joint probability density function ρ and image set $\Xi \subset \mathbb{R}^N$, where we assume in this section for brevity of notation that Ξ is given as the hypercube $[-1, 1]^N$. Note that different image sets Ξ or stochastic dependence could also be considered, for example, by an isoprobabilistic transformation.[17] Additionally, we assume that the map $\mathcal{Q}: \Xi \to \mathbb{C}$ is holomorphic. Note that this assumption can often be justified for boundary value problems with random influences, see, for example, Ref.[18] Holomorphy of the solution of Maxwell's source problem with respect to general shape parametrizations was established in Ref.[19]

As discussed in the following, in this work we propose a method for surrogate modeling, where the basis functions are mapped polynomials based on gPC[7] combined with a mapping, which is conformal in each coordinate. To compute the corresponding coefficients we rely on pseudo-spectral projection based on mapped quadrature rules.[8]

3.1 | Generalized polynomial chaos

For convenience of the reader, we briefly recall the standard polynomial chaos expansions, going back to Wiener.[20] Considering Gaussian random variables, any $\mathcal{Q}(\mathbf{y})$ with bounded variance, can be accurately represented using Hermite polynomials as basis functions. Employing the Askey-Scheme,[7] for different probability distributions ρ, basis functions $\Psi_m: \Xi \to \mathbb{R}$ which are orthonormal w.r.t. the probability density ρ, that is,

$$\mathbb{E}\left[\Psi_i \Psi_j\right] := \int_{\Xi} \Psi_i(\mathbf{y}) \Psi_j(\mathbf{y}) \rho(\mathbf{y}) \mathrm{d}\mathbf{y} = \delta_{ij}, \tag{8}$$

can be obtained. We note that gPC can also be constructed for arbitrary densities ρ.[21] Moreover, the gPC expansion converges for every square-integrable function if the support of the density is compact, for instance, see Ref.,[22] theorem 3.4. In this respect, we consider arbitrary densities on $[-1, 1]^N$. The gPC approximation is then given as

$$\mathcal{Q}_M^{\mathrm{PC}}(\mathbf{y}) = \sum_{m=0}^{M} s_m \Psi_m(\mathbf{y}), \tag{9}$$

where the $s_m \in \mathbb{C}$ denote the gPC coefficients. The sum in Equation (9) has already been truncated to $M < \infty$ to obtain a computable approximation and hence, limited polynomial degrees are considered. The coefficients s_m can then be determined in various ways, for example, by regression or stochastic collocation, see Ref.[23] for an overview. Here we consider projection, that is

$$s_m = \mathbb{E}[\mathcal{Q}\Psi_m] = \int_{\Xi} \mathcal{Q}(\mathbf{y})\Psi_m(\mathbf{y})\rho(\mathbf{y})\mathrm{d}\mathbf{y}. \tag{10}$$

The integral in Equation (10) is usually not readily computable and is hence often approximated by numerical quadrature. Due to orthogonality of the basis, stochastic moments as well as variance-based sensitivity indices can then be calculated directly from the coefficients s_m without further approximations, see Ref.[23] These methods show spectral convergence, for example, in the norm $\|u\|_{L^2_\rho} \coloneqq \sqrt{\mathbb{E}[u^2]}$.[7] In particular, if the map $\mathbf{y} \mapsto \mathcal{Q}(\mathbf{y})$ is analytic, exponential convergence can be expected, as discussed in the following. Note that, for simplicity, we first consider the univariate case, that is, $N = 1$, while generalizations to the multivariate case $N > 1$ will be discussed later.

We assume that $\mathcal{Q}_{1\mathrm{D}} : [-1,1] \to \mathbb{C}$ can be analytically extended onto an open Bernstein ellipse $E_r \subset \mathbb{C}$. A Bernstein ellipse E_r is an ellipse with foci at ± 1 and the size r is given by the sum of the length of semi-major and semi-minor axis. This is illustrated in Figure 2A. Following Ref.,[9] the error of the polynomial best approximation $\mathcal{Q}_M^{\mathrm{pol}^*}$ with degree M can be estimated as

$$\left\| \mathcal{Q}_{1\mathrm{D}} - \mathcal{Q}_M^{\mathrm{pol}^*} \right\|_\infty \leq \frac{C_{\mathrm{B}} e^{-\log(r)M}}{r-1}, \tag{11}$$

where $\|\cdot\|_\infty$ denotes the supremum-norm on $[-1, 1]$ and the constant $C_{\mathrm{B}} > 0$ depends on the uniform bound of $\mathcal{Q}_{1\mathrm{D}}$ in E_r. It can be seen that the asymptotic rate of geometric convergence (Ref.,[24] definition 6) is given by the factor $\log r$ and, hence, a large region of analyticity is desirable. Note that convergence in the supremum-norm implies convergence in the $\|\cdot\|_{L^2_\rho}$ norm as well, as

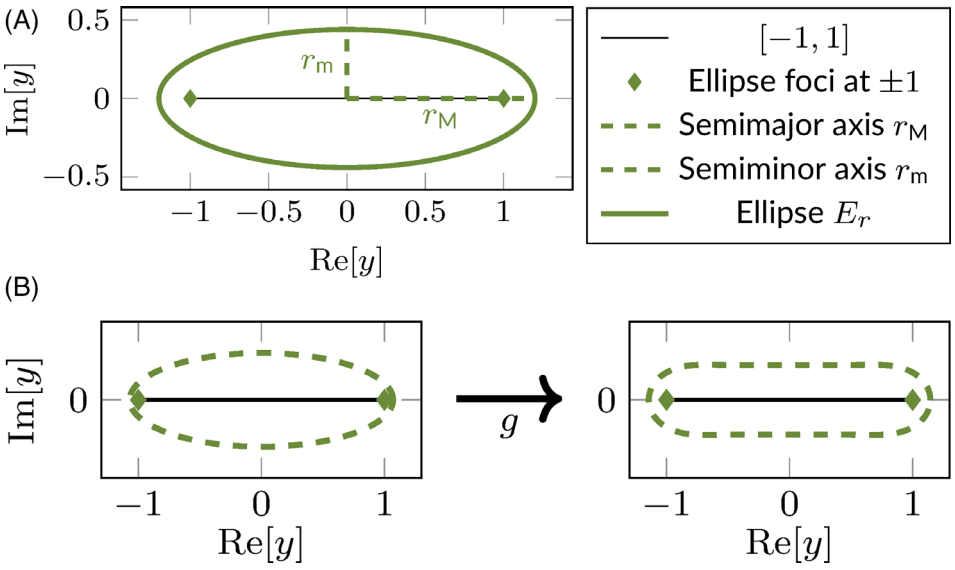

FIGURE 2 Illustration of conformal mapping approach based on Ref.[11]. A, Bernstein ellipse E_r of size $r = r_M + r_m$. B, Conformal map of a Bernstein ellipse E_r to a *straighter* region $g(E_r)$

$$\left\| \mathcal{Q}_{1D} - \mathcal{Q}_M^{\text{pol}^*} \right\|_{L^2_\rho} = \left(\int_{[-1,1]} \left(\mathcal{Q}_{1D} - \mathcal{Q}_M^{\text{pol}^*} \right)^2 \rho_{1D} \mathrm{d}y \right)^{\frac{1}{2}} \leq \left\| \sqrt{\rho_{1D}} \right\|_\infty \left\| \mathcal{Q}_{1D} - \mathcal{Q}_M^{\text{pol}^*} \right\|_\infty \left(\int_{[-1,1]} 1 \mathrm{d}y \right)^{\frac{1}{2}} = \sqrt{2} \left\| \sqrt{\rho_{1D}} \right\|_\infty \left\| \mathcal{Q}_{1D} - \mathcal{Q}_M^{\text{pol}^*} \right\|_\infty. \tag{12}$$

We further note that the additional aliasing error introduced by the discrete projection can be controlled so that it does not harm the convergence order for a well-resolved smooth function (cf. Ref.[7] chapter 3.6).

3.2 | Conformally mapped generalized polynomial chaos

Equation (11) shows that the convergence is connected to the region of analyticity, in particular the convergence rate $\log r$ depends on the size of the largest Bernstein ellipse not containing any poles of the continuation of $\mathcal{Q}_{1D}$ (in the complex plane). However, established procedures[25] inferring the regularity of parametric problems based on a sensitivity analysis, do not lead to elliptical regions, but rather prove analyticity in an ϵ-neighborhood of the unit interval. In this case, a conformal map g can be employed, which maps Bernstein ellipses to *straighter* regions and thus, enlarges the domain of analyticity, as illustrated in Figure 2B. To this end, there are various mappings which could be employed, cf. Ref.[26] Here, we focus for simplicity on the so-called sausage mapping introduced in Ref.[8] It represents a Taylor approximation of the inverse sine function, which is then normalized such that $g(\pm 1) = \pm 1$ is fulfilled. In particular, we employ the 9-th order mapping, that is,

$$g(s) = \frac{1}{53089} \left(40320s + 6720s^3 + 3024s^5 + 1800s^7 + 1225s^9 \right), \tag{13}$$

as it has already been established in the recent works[8,11,26] and fulfills the intended properties for a substantial range of epsilon neighborhoods, see, for example, Ref.,[8] theorem 4 or Ref.,[11] Figure 7B. A detailed comparison of different mappings is out of the scope of this paper. Note that g maps the unit interval to itself, that is

$$g([-1,1]) = [-1,1]. \tag{14}$$

Conformal maps were employed in Ref.[8] to derive new numerical quadrature formulas, and have also recently been considered in the context of stochastic collocation methods.[10,11] In this work, we address the combination of conformal maps and polynomial chaos expansions. Based on the assumption that $h := \mathcal{Q}_{1D} \circ g$ has a larger Bernstein ellipse than $\mathcal{Q}_{1D}$, and is hence better suited to be approximated with polynomials, we propose a new orthogonal basis

$$\Phi_m := \tilde{\Psi}_m \circ g^{-1}, \quad m = 0, \ldots, M, \tag{15}$$

where $\tilde{\Psi}_m$ are orthonormal polynomials w.r.t. the transformed density

$$\tilde{\rho}_{1D}(s) := g'(s) \rho_{1D}(g(s)). \tag{16}$$

We emphasize that $\{\Phi_m\}_{m=0}^M$ forms an orthonormal basis w.r.t. the input probability distribution ρ. This can be shown by a change of variables $y = g(s)$

$$\mathbb{E}\left[\Phi_i \Phi_j\right] = \int_{-1}^{1} \left(\tilde{\Psi}_i \circ g^{-1} \right)(y) \left(\tilde{\Psi}_j \circ g^{-1} \right)(y) \rho_{1D}(y) \mathrm{d}y \tag{17}$$

$$= \int_{-1}^{1} \tilde{\Psi}_i(s) \tilde{\Psi}_j(s) \underbrace{\rho_{1D}(g(s)) g'(s)}_{\tilde{\rho}_{1D}(s)} \mathrm{d}s = \delta_{ij}, \tag{18}$$

where the last line holds by construction of the polynomials $\tilde{\Psi}_m$. Due to the orthogonality, the corresponding coefficients s_m of the mapped approximation

$$Q_M(y) = \sum_{m=0}^{M} s_m \Phi_m(y) \tag{19}$$

can then be determined by the projection

$$s_m = \mathbb{E}[\Phi_m Q_{1D}] = \int_{-1}^{1} \Phi_m(y) Q_{1D}(y) \rho_{1D}(y) \mathrm{d}y. \tag{20}$$

Note that, by abuse of notation, we use the same symbol s_m for the gPC coefficients and the mapped gPC coefficients. The mapped polynomial best approximation $\mathcal{Q}_M^*$ converges as

$$\left\| \mathcal{Q}_{1D} - \mathcal{Q}_M^* \right\|_\infty = \left\| \mathcal{Q}_{1D} \circ g - \mathcal{Q}_M^* \circ g \right\|_\infty = \left\| \left(h - h_M^{\mathrm{pol}^*} \right) \right\|_\infty \leq \frac{\tilde{C}_B e^{-\log(\tilde{r})M}}{\tilde{r}-1}, \tag{21}$$

where $h_M^{\mathrm{pol}^*}$ denotes the polynomial best approximation of h and $\tilde{r}$ the size of a Bernstein ellipse $E_{\tilde{r}}$ on which an analytic continuation of h exists.

In particular, the asymptotic rate of geometric convergence $\log\tilde{r}$ of the mapped approximation $\mathcal{Q}_M$ depends on the size of the largest Bernstein ellipse $E_{\tilde{r}_{\max}}$ which is fully mapped into the region of analyticity of $\mathcal{Q}_{1D}(y)$. Note that $\tilde{r}_{\max} > r_{\max}$ for any positive $\varepsilon < 0.75$,[11] and hence, a convergence improvement is to be expected in those cases, that is, for functions analytic in such ε-neighborhoods. It should be mentioned nevertheless that this procedure does not always yield improved convergence rates. One can easily imagine poles located such that a Bernstein ellipse may lead to a larger region of analyticity than a strip-like geometry. In the examples considered in this work, however, convergence acceleration could indeed be obtained.

To numerically compute Equation (20), we derive mapped quadrature rules, cf. Refs.[8,26] As pointed out in Ref.[9] for instance, Gaussian quadrature is derived from polynomial approximations and, hence, the convergence order also depends on the size of the Bernstein ellipse corresponding to the regularity of the integrand, see for example, Ref.,[8] theorem 1. Therefore, relying again the assumption that $\mathcal{Q}_{1D} \circ g$ has a larger Bernstein ellipse, we apply a change of variables $y = g(s)$ in Equation (20)

$$s_m = \mathbb{E}[\Phi_m \mathcal{Q}_{1D}] = \int_{-1}^{1} \Phi_m(y) \mathcal{Q}_{1D}(y) \rho_{1D}(y) \mathrm{d}y = \int_{-1}^{1} \Phi_m(g(s)) \mathcal{Q}_{1D}(g(s)) \underbrace{\rho_{1D}(g(s)) g'(s)}_{\tilde{\rho}_{1D}} \mathrm{d}s. \tag{22}$$

The mapped quadrature scheme is then obtained by application of Gaussian quadrature w.r.t. the transformed density $\tilde{\rho}_{1D}$, that is, quadrature nodes $\left\{\tilde{y}^{(i)}\right\}_{i=0}^{M_{\mathrm{quad}}}$ and correspondings weights $\left\{\tilde{w}^{(i)}\right\}_{i=0}^{M_{\mathrm{quad}}}$, to the transformed integrand in Equation (22)

$$s_m \approx \sum_{i=0}^{M_{\mathrm{quad}}} \Phi_m\left(g\left(\tilde{y}^{(i)}\right)\right) \mathcal{Q}_{1D}\left(g\left(\tilde{y}^{(i)}\right)\right) \tilde{w}^{(i)} = \sum_{i=0}^{M_{\mathrm{quad}}} \Phi_m\left(\hat{y}^{(i)}\right) \mathcal{Q}_{1D}\left(\hat{y}^{(i)}\right) \hat{w}^{(i)}. \tag{23}$$

Note that the mapped quadrature nodes are obtained as $\hat{y}^{(i)} := g\left(\tilde{y}^{(i)}\right)$, while the mapped weights are given as $\hat{w}^{(i)} := \tilde{w}^{(i)}$. Due to Equation (14), it is ensured that the mapped quadrature nodes $\hat{y}^{(i)}$ do not require the evaluation of the analytic continuation of $\mathcal{Q}_{1D}$ in the complex plane, which is, in practice, not always possible. A convergence improvement is expected based on the assumption that the transformed integrand in Equation (22) has a larger Bernstein ellipse. For further details on mapped quadrature schemes, we refer to Ref.[8] However, we note the (minor) difference that in this work we employ Gaussian quadrature w.r.t. the transformed density $\tilde{\rho}_{1D}$ to derive the mapped quadrature scheme, while Ref.[8] only considers unweighted Gaussian quadrature and, thereby, takes $g'(s)$ as part of the integrand (instead of the weight).

We proceed with a discussion of the multivariate case $N > 1$. To this end, we introduce the multivariate mapping $\mathbf{g}(\mathbf{s}) = [g_1(s_1),..., g_N(s_N)]$, which is assumed to be conformal in each coordinate s_i. In this work, we employ, for simplicity, the same mapping (13) for all parameters, that is, $g_1 = \ ... \ = g_N = g$. However, different choices would be possible as well. We also note that, for the trivial mapping $\mathbf{g}_{\text{triv}} : \mathbf{s} \mapsto \mathbf{s}$ standard polynomial chaos expansions would be recovered. For each parameter y_i with univariate probability density function (PDF) ρ_i, we define the transformed PDF $\tilde{\rho}_i(y_i) := \rho_i(g_i(y_i))g'_i(y_i)$. The corresponding transformed joint PDF is then given by $\tilde{\rho}(\mathbf{y}) = \tilde{\rho}_1(y_1) ... \tilde{\rho}_N(y_N)$. In the following, we denote by $\left\{\tilde{\Psi}_{\mathbf{m}}\right\}_{\mathbf{m}}$ an orthonormal polynomial basis w.r.t. to the transformed density $\tilde{\rho}$, that is,

$$\mathbb{E}_{\tilde{\rho}}\left[\tilde{\Psi}_{\mathbf{i}}\tilde{\Psi}_{\mathbf{j}}\right] := \int_{\Xi} \tilde{\Psi}_{\mathbf{i}}(\mathbf{y})\tilde{\Psi}_{\mathbf{j}}(\mathbf{y})\tilde{\rho}(\mathbf{y})\mathrm{d}\mathbf{y} = \delta_{i_1 j_1} ... \delta_{i_N j_N}, \tag{24}$$

where we introduced the multi-index $\mathbf{m} = (m_1, ..., m_N)$ holding the univariate polynomial degrees, such that $\tilde{\Psi}_{\mathbf{m}}$ is a tensor-product polynomial of order m_j in dimension $j = 1, ..., N$. The respective mapped polynomials are then obtained as

$$\Phi_{\mathbf{m}}(\mathbf{y}) := \left(\tilde{\Psi}_{\mathbf{m}} \circ \mathbf{g}^{-1}\right)(\mathbf{y}). \tag{25}$$

The coefficients of the multivariate mapped approximation

$$\mathcal{Q}_p(\mathbf{y}) := \sum_{\|\mathbf{m}\|_\infty \leq p} s_{\mathbf{m}}\Phi_{\mathbf{m}}(\mathbf{y}), \tag{26}$$

where we consider for simplicity a tensor-product construction of maximum degree p, can then again be obtained by projection

$$s_{\mathbf{m}} = \mathbb{E}[\Phi_{\mathbf{m}}\mathcal{Q}] = \int_{\Xi} \Phi_{\mathbf{m}}(\mathbf{y})\mathcal{Q}(\mathbf{y})\rho(\mathbf{y})\mathrm{d}\mathbf{y}. \tag{27}$$

To evaluate the multi-dimensional integral in Equation (27), we employ mapped Gaussian quadrature. In this case the mapped nodes and weights are given by $\hat{\mathbf{y}}^{(i)} := \mathbf{g}\left(\tilde{\mathbf{y}}^{(i)}\right)$ and $\hat{w}^{(i)} := \tilde{w}^{(i)}$, respectively, where, in turn, $\tilde{\mathbf{y}}^{(i)}$ and $\tilde{w}^{(i)}$ are the nodes and weights of a Gaussian quadrature w.r.t. $\tilde{\rho}$.

Finally, we emphasize that, since the mapped representation (26) uses an orthogonal basis, the coefficients $s_{\mathbf{m}}$ can be used to directly compute stochastic moments as well as variance-based sensitivity indices. For instance, the mean value is given by

$$\mathbb{E}\left[\mathcal{Q}_p\right] = \int_{\Xi} \left(\sum_{\|\mathbf{m}\|_\infty \leq p} s_{\mathbf{m}}\Phi_{\mathbf{m}}(\mathbf{y}) \right) \rho(\mathbf{y})\mathrm{d}\mathbf{y} = s_{\mathbf{0}}, \tag{28}$$

where we employed, that the mapped basis function $\Phi_{\mathbf{0}}$ is constant on Ξ, as well as the orthonormality condition (24). Accordingly the variance is given by

$$\mathbb{V}\left[\mathcal{Q}_p\right] = \mathbb{E}\left[\mathcal{Q}_p^2\right] - \mathbb{E}\left[\mathcal{Q}_p\right]^2 = \sum_{0 < \|\mathbf{m}\|_\infty \leq p} s_{\mathbf{m}}^2. \tag{29}$$

Additionally, Sobol sensitivity indices,[27] based on a decomposition of the variance, can also be directly derived from the coefficients. Regarding the estimation of Sobol indices, we will focus on the so-called main-effect (1st order) and total-effect (total order) indices. We define the multi-index sets $\Lambda_n^{\text{main}}, \Lambda_n^{\text{total}} \subset \Lambda_p^{\text{TP}} := \left\{\mathbf{m} | 0 \leq \|\mathbf{m}\|_\infty \leq p\right\}$, $n = 1, 2, ..., N$, such that

$$\Lambda_n^{\text{main}} = \left\{ \mathbf{m} \in \Lambda_p^{\text{TP}} \ : \ m_n \neq 0 \text{ and } m_j = 0, n \neq j \right\}, \tag{30}$$

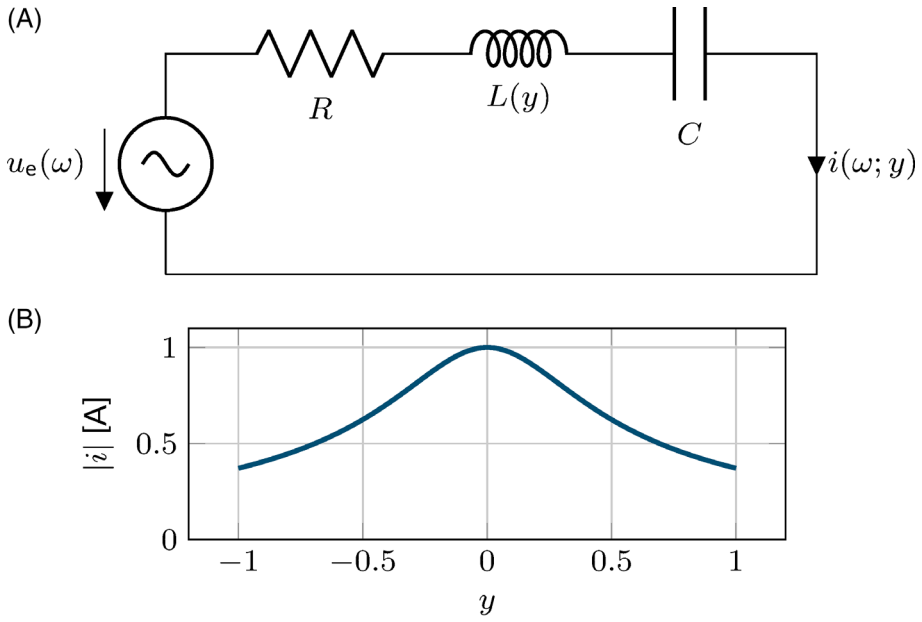

FIGURE 3 Benchmark problem: RLC circuit. A, Circuit diagram. B, Amplitude of electric current w.r.t. input parameter y

$$\Lambda_n^{\text{total}} = \left\{ \mathbf{m} \in \Lambda_p^{\text{TP}} \ : \ m_n \neq 0 \right\}. \tag{31}$$

We then define the partial variances $\mathbb{V}_n^{\text{main}}[\mathcal{Q}_p]$ and $\mathbb{V}_n^{\text{total}}[\mathcal{Q}_p]$, such that

$$\mathbb{V}_n^{\text{main}}[\mathcal{Q}_p] = \sum_{\mathbf{m} \in \Lambda_n^{\text{main}}} s_{\mathbf{m}}^2, \qquad \mathbb{V}_n^{\text{total}}[\mathcal{Q}_p] = \sum_{\mathbf{m} \in \Lambda_n^{\text{total}}} s_{\mathbf{m}}^2. \tag{32}$$

Then, the main-effect and total-effect Sobol indices, S_n^{main} and S_n^{total}, respectively, are given as

$$S_n^{\text{main}}[\mathcal{Q}_p] = \frac{\mathbb{V}_n^{\text{main}}[\mathcal{Q}_p]}{\mathbb{V}[\mathcal{Q}_p]}, \qquad S_n^{\text{total}} = \frac{\mathbb{V}_n^{\text{total}}[\mathcal{Q}_p]}{\mathbb{V}[\mathcal{Q}_p]}. \tag{33}$$

4 | APPLICATION

We apply the UQ methods presented in the last section to two model problems. We first consider an academic example of a stochastic RLC circuit, since there is a closed-form solution available which allows us to illustrate the main ideas of the proposed approach in detail. We then consider the optical grating coupler,[2] which is a non-trivial benchmark example from nanoplasmonics.

4.1 | RLC circuit

We consider the model of an RLC circuit, as illustrated in Figure 3A. Assuming harmonic time dependency, the electric current i is given by

$$\left(-L\omega^2 + j\omega R + \frac{1}{C} \right) i = j\omega u_e. \tag{34}$$

We consider, arbitrarily chosen, an angular frequency $\omega = 10^4\ \text{s}^{-1}$, excitation voltage $u_e = 1$ V, capacitance $C = 10\ \mu$F, and a (rather small) resistance of $R = 1\ \Omega$. Additionally, we consider a variable inductance $L(y) = 1\ \text{mH} + 0.25\ \text{mH} \cdot y$. The parameter y is then modeled as a uniformly distributed random variable with probability density function $\rho = 1/2$, on $[-1,1]$ such that a stochastic model is obtained. As QoI $\mathcal{Q}$, we consider the amplitude of the current $\mathcal{Q} := |i|$.

Figure 3B shows the parametric dependency of the QoI $|i|$ with respect to y, which is analytic for $y \in [-1, 1]$. However, the continuation in the complex plane has poles at

$$y = \pm i \frac{R}{\omega \cdot 0.25\,\mathrm{mH}}. \tag{35}$$

This complex conjugate pole pair limits the size of the largest Bernstein ellipse, where $\mathcal{Q}(y)$ is analytic, which is illustrated in Figure 4A for different values of R.

In each case, we compute gPC approximations of increasing order for $\mathcal{Q}(y)$ using the Chaospy toolbox.[28] In particular, the gPC coefficients of an $M-$th order approximation are computed by pseudo-spectral projection using Gaussian quadrature of order $M+1$. The accuracy of the surrogate models is then quantified in the empirical L^2_ρ norm. More precisely, we apply cross-validation using $N^{\mathrm{cv}} = 1000$ random parameter realizations $y_{\mathrm{cv}}^{(i)}$ drawn according to the probability density ρ, to compute the error

$$E^{\mathrm{cv}} = \frac{1}{N^{\mathrm{cv}}} \sum_{i=1}^{N^{\mathrm{cv}}} \left| \mathcal{Q}_M^{\mathrm{PC}}\left(y_{\mathrm{cv}}^{(i)}\right) - \mathcal{Q}\left(y_{\mathrm{cv}}^{(i)}\right) \right|^2. \tag{36}$$

Additionally, we compute the error in the first-stochastic moment, that is, the mean value of the gPC approximation given by the first polynomial coefficient s_0. The reference solutions for the expected values are obtained by Gaussian quadrature of order 200 up to machine accuracy. The convergence of the corresponding surrogate model w.r.t. the polynomial order M, in terms of cross-validation and mean value accuracy, are presented in Figure 4B,C, respectively. The

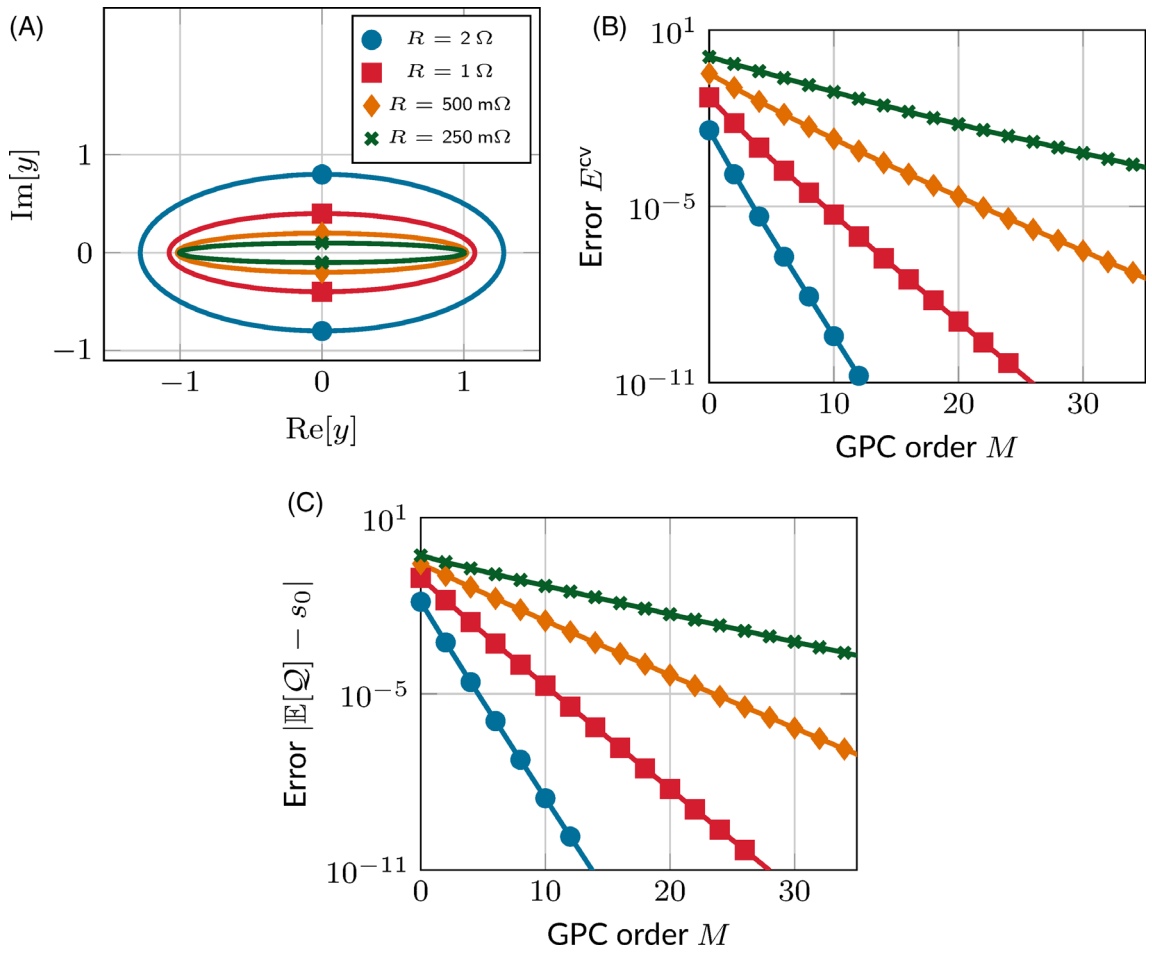

FIGURE 4 Illustration of influence of poles in complex plane (RLC circuit). A, Poles of $\mathcal{Q}(y)$ and corresponding Bernstein ellipses for different R. B, Convergence of empirical L^2 error. C, Convergence of mean of GPC approximation

plots confirm Equation (11) numerically, showing a decreasing convergence order for decreasing values of R corresponding to decreasing sizes of the associated Bernstein ellipses. Note that, according to Equation (35), a similar behavior as for decreasing damping can be expected for increasing amplitudes of the considered input variation.

Next, we apply the conformally mapped gPC expansions proposed in the last section. The implementation is done in Python based on Chaospy.[28] Figure 5A shows the transformed density (16) for a uniform input distribution ρ. Figure 5B depicts some exemplary basis functions of gPC and mapped gPC. Note that the gPC basis functions are in this case Legendre polynomials, while the mapped basis functions, given by Equation (15), are no polynomials. We then study the convergence of the corresponding surrogate models, where mapped quadrature of order $M + 1$ is used to compute the mapped gPC expansions of order M. Figure 5C-E demonstrate the improved convergence order of the mapped approach, in terms of the cross-validation error, as well as the accuracy of the computed mean value and the computed standard deviation (SD).

4.2 | Optical grating coupler

We now consider the FE model of an optical grating coupler,[2] which was introduced in the beginning, see Figure 1A. The structure's design[29] is shown in Figure 6. A plane wave at optical frequency hits the surface of the grating coupler. The incident wave couples with a MIM plasmon mode, which propagates along the metallic surface. It is found that the

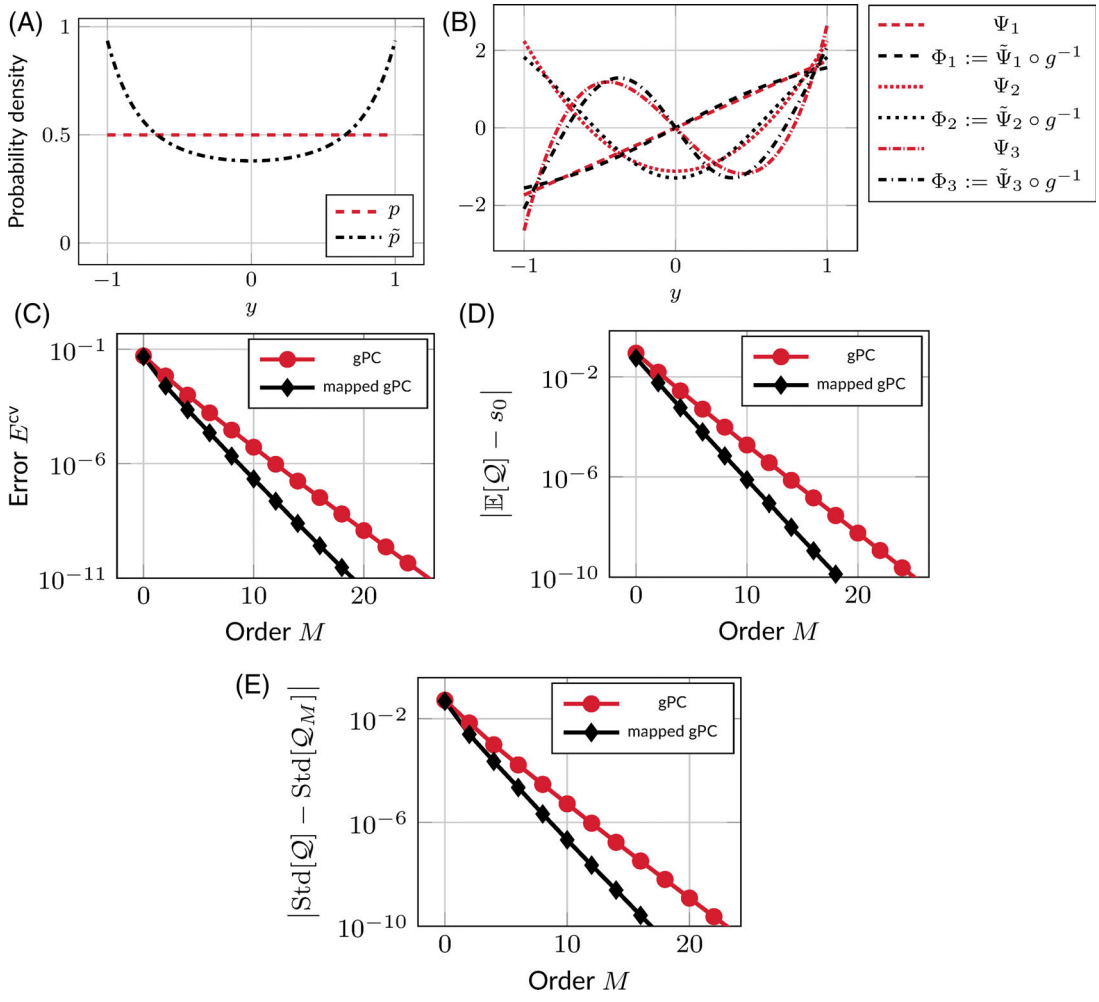

FIGURE 5 (Mapped) Generalized polynomial chaos (gPC) for stochastic RLC circuit with $R = 1\ \Omega$. A, Uniform input distribution and associated transformed density $\tilde{p}$. B, Some basis functions for gPC and mapped gPC. C, Convergence of empirical L^2_ρ error. D, Convergence of mean value. E, Convergence of SD

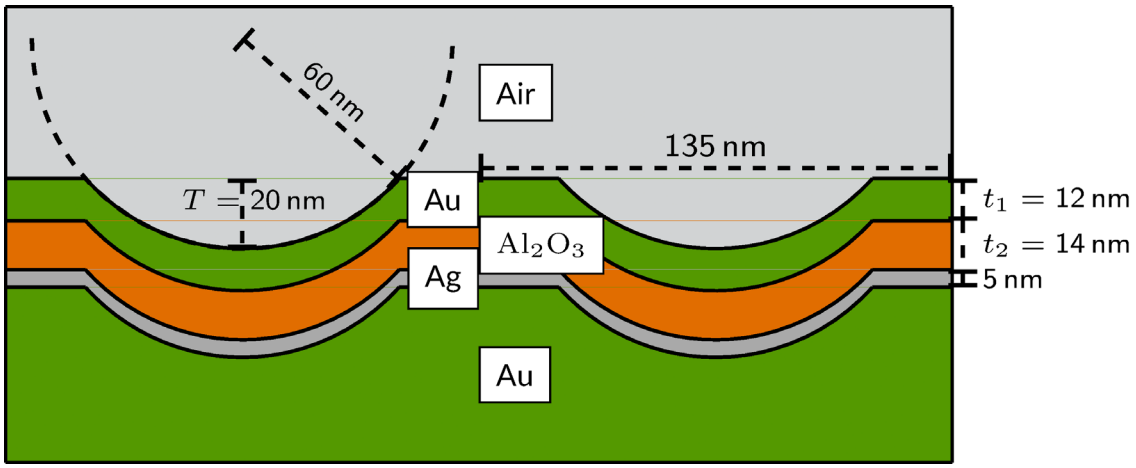

FIGURE 6 Numerical model of an optical grating coupler based on Ref.[11]. Excitation by incident plane wave at upper boundary

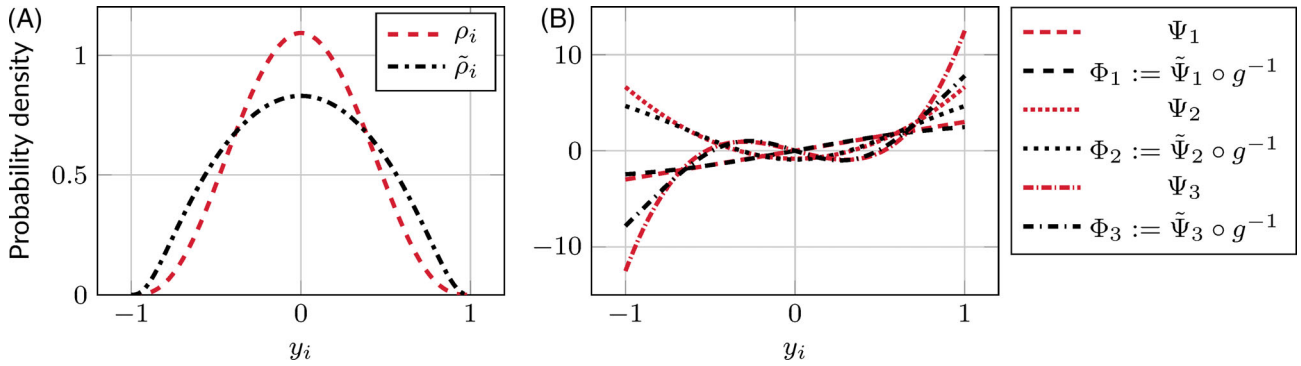

FIGURE 7 gPC for stochastic RLC circuit with beta distributed input parameter. A, Beta input distribution ρ_i and associated transformed density $\tilde{\rho}_i$. B, Some univariate basis functions for gPC and mapped gPC

MIM resonance has a significant shift (in energy) as a function of the grating depth[2] and therefore, it is of great interest to evaluate the influence of nano-technological manufacturing imperfections.

We use FENICS[30] for the discretization and implement a design element approach[31] for the geometry parametrization. The numerical model is described in greater detail in Ref.[11] Note that we only consider periodic variations, modeling a systematic offset in the fabrication process, and do not address local uncertainties leading to different unit cells. Readers interested in the latter case are referred to Ref.[32] The fundamental scattering parameter is considered as QoI $\mathcal{Q}(\mathbf{y}) \in \mathbb{C}$. We consider three sensitive geometrical parameters as uncertain, in particular the thicknesses of the upper gold layer $t_1 = 12\,\text{nm} + \Delta y_1$, the thickness of the dielectric layer $t_2 = 14\,\text{nm} + \Delta y_2$ and the grating depth $T = 20\,\text{nm} + \Delta y_3$, as illustrated in Figure 6. We model those parameters as independent beta distributed RVs in the range of $\pm\Delta = \pm 2$ nm. The corresponding shape parameters are chosen such that a normal distribution is approximated. The corresponding probability distribution ρ_i of the RVs y_i, $i = 1, \ldots, 3$ is shown in Figure 7A, together with the transformed density $\tilde{\rho}_i$. The univariate gPC polynomials which are Jacobi polynomials in this case, as well as the mapped polynomials are illustrated in Figure 7B.

4.2.1 | Decay of Fourier coefficients

We first study the decay of polynomial coefficients to numerically investigate the smoothness of the mapping from the input parameters to the complex S-parameter $\mathcal{Q}$ and justify the use of (mapped) polynomial approximations. It has been

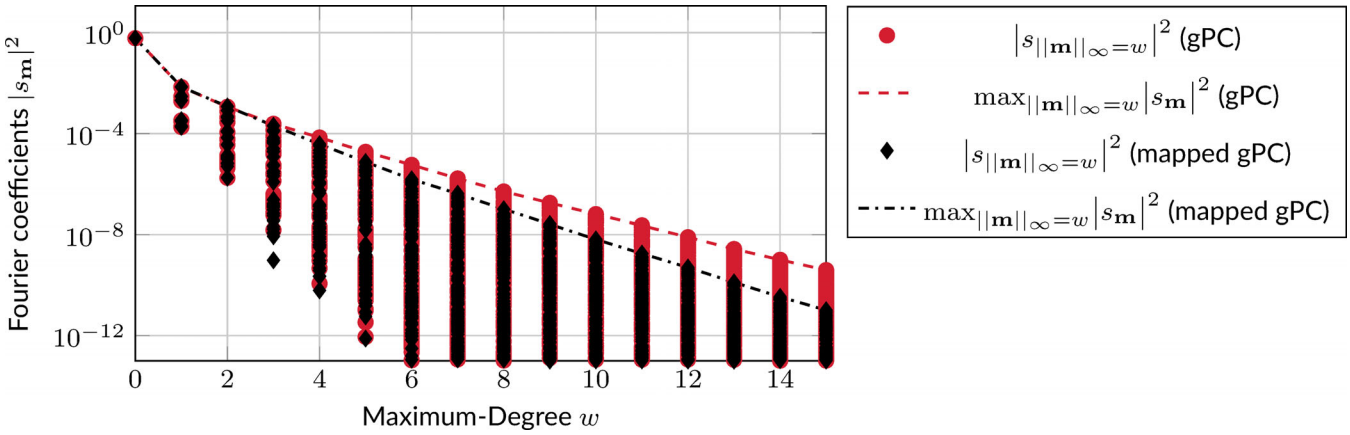

FIGURE 8 Decay of Fourier coefficients of multivariate (mapped) gPC approximation

shown, see for example, Ref.,[33] lemma 2 where Legendre polynomials are considered, that if this mapping is analytic, the Fourier coefficients $s_{\mathbf{m}}$ of an $N-$variate gPC approximation decay exponentially. In particular,

$$|s_{\mathbf{m}}|^2 \leq Ce^{-\sum_{n=1}^{N} g_n m_n}, \tag{37}$$

where C and g_n, $n = 1,\ldots, N$ are positive constants independent of $\mathbf{m}$ and where we have assumed that the polynomials are normalized. We consider the maximum of the absolute value of the Fourier coefficients $s_{\mathbf{m}}$ with fixed maximum-degree w

$$\max_{\|\mathbf{m}\|_\infty = w} |s_{\mathbf{m}}|^2 \leq \max_{\|\mathbf{m}\|_\infty = w} Ce^{-\sum_{n=1}^{N} g_n m_n} = Ce^{-\min_{\|\mathbf{m}\|_\infty = w} \sum_{n=1}^{N} g_n m_n} \leq Ce^{-(\min_n g_n) w}. \tag{38}$$

It can be seen that the maximum Fourier coefficient is expected to decay exponentially with an increasing maximum-degree w.

We construct a multivariate gPC approximation with a tensor-product basis of order $m_{\max} = 15$. The multivariate integrals of the pseudo-spectral projection are then computed by a Gauss quadrature of order 17. All coefficients $s_{\mathbf{m}}$ are plotted in Figure 8 in red color, where an exponential decay can indeed be observed. This can be seen as a numerical indicator for smoothness of the approximated mapping $\mathcal{Q}(\mathbf{y})$. Additionally, we also construct a mapped approximation of same order and plot the corresponding coefficients in black color. It can be observed that the mapped coefficients exhibit a faster convergence and hence the mapped approach can be expected to show, again, an improved convergence.

4.2.2 | Uncertainty quantification

Next, we consider approximations of the magnitude of the S-parameter $|\mathcal{Q}(\mathbf{y})|$ using (mapped) tensor-product gPC expansions of increasing order M, where pseudo-spectral projections of order $M + 1$ is employed to compute the coefficients. Figure 9A compares gPC and the proposed mapped counterpart in terms of the L^2_ρ-error (36), in particular, again, by cross-validation with 10^3 random parameter realizations. It can be observed that the mapped approach converges about 30% faster w.r.t. the order M than gPC. However, the respective computational gain grows, in this case, exponentially w.r.t. the number of inputs and, hence, the required number of model evaluation to reach a prescribed accuracy reduces roughly by a factor of 2. Similar findings hold for the stochastic moments, in particular, we present the convergence of the mean value in Figure 9B and the computed SD in Figure 9C. In this case, the reference solutions are obtained by Gaussian quadrature of order 30.

Finally, the most accurate surrogate model, that is, the mapped gPC expansion of order 14, is used to compute the mean value $\mathbb{E}[|\mathcal{Q}|] \approx 0.786$ and the SD $\sqrt{\mathbb{V}[|\mathcal{Q}|]} \approx 0.077$ of the QoI. Additionally, Sobol indices are computed and presented in Figure 10. The thickness of the dielectric layer t_2 is identified as the most influential parameter. We note that

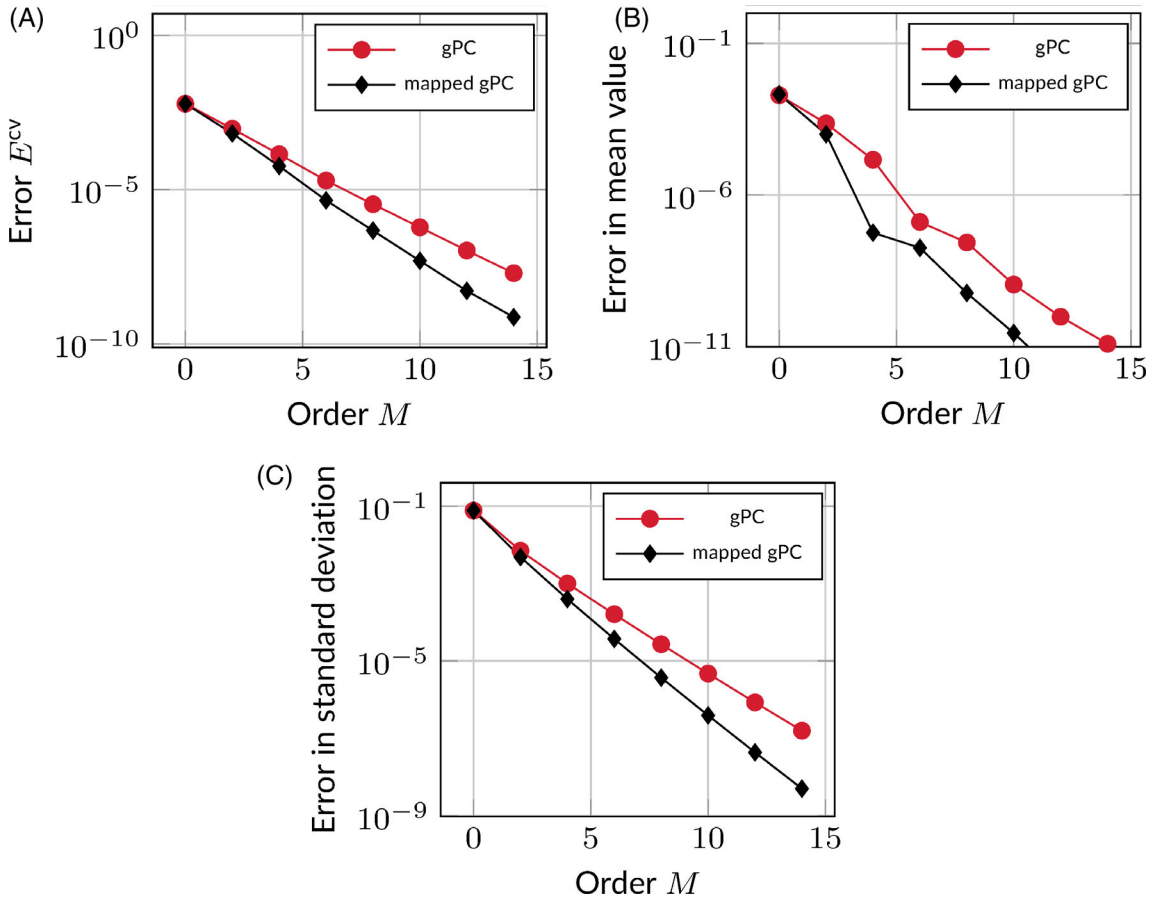

FIGURE 9 Convergence of (mapped) gPC expansions for the optical grating coupler. A, Convergence of empirical L^2_ρ error. B, Convergence of mean value. C, Convergence of SD

FIGURE 10 Sensitivity of input parameters

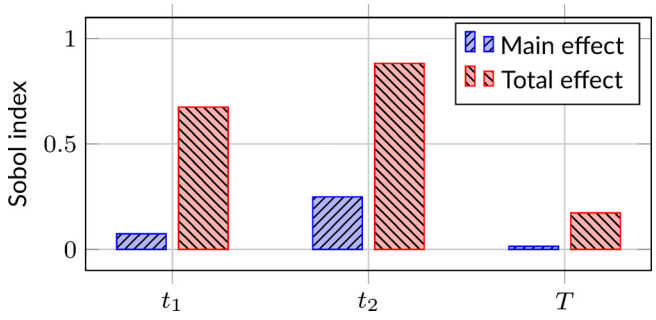

there is a significant difference between the main- and total-effect indices. In particular, the sum of the first order indices is only 34%, while the remaining 66% can be attributed to strong coupling effects among the parameters.

5 | CONCLUSIONS

In this paper an efficient surrogate modeling technique for quantifying uncertainties in the material and geometry of high-frequency and optical devices was presented. The proposed method is based on gPC to achieve spectral convergence. Through a combination with conformal maps we were able to enlarge the region of analyticity. This led to an improved convergence rate, which was numerically demonstrated for two benchmark problems. In particular, the approach showed significant gains in either accuracy or computational cost, requiring only minor modifications of an

existing code. Due to orthogonality of the proposed basis, stochastic moments as well as Sobol indices can be directly obtained from the coefficients. It is worth noting that this technique can also be combined with other techniques for convergence acceleration such as adjoint-error correction, sparse-grids and (adjoint-based) adaptivity for the multivariate case.[11]

ACKNOWLEDGEMENTS

This research was funded by the Deutsche Forschungsgemeinschaft (DFG, German Research Foundation) - RO4937/1-1. The work of Niklas Georg is also partially funded by the Excellence Initiative of the German Federal and State Governments and the Graduate School of Computational Engineering at Technische Universität Darmstadt (DFG GSC 233).

ORCID

Ulrich Römer https://orcid.org/0000-0002-1277-7509

REFERENCES

1. Xiu D. Fast numerical methods for stochastic computations: a review. *Commun Comput Phys*. 2009;5(2-4):242-272.
2. Preiner MJ, Shimizu KT, White JS, Melosh NA. Efficient optical coupling into metal-insulator-metal plasmon modes with subwavelength diffraction gratings. *Appl Phys Lett*. 2008;92(11):113109. https://doi.org/10.1063/1.2898509.
3. Le MaitreOP, Knio OM. *Spectral Methods for Uncertainty Quantification: With Applications to Computational Fluid Dynamics*. Netherlands: Springer; 2010.
4. Austin ACM, Sarris CD. Efficient analysis of geometrical uncertainty in the FDTD method using polynomial chaos with application to microwave circuits. *IEEE Trans Microwave Theory Tech*. 2013;61(12):4293-4301. https://doi.org/10.1109/TMTT.2013.2281777.
5. Georg N, Ackermann W, Corno J, Schöps S. Uncertainty quantification for Maxwell's eigenproblem using isogeometric analysis and mode tracking. *Comput Methods Appl Mech Eng*. 2019;350:228-244. https://doi.org/10.1016/j.cma.2019.03.002.
6. Corno J, Georg N, Gorgi Zadeh S, et al. Uncertainty modeling and analysis of the European X-ray free electron laser cavities manufacturing process. *Nucl Instrum Meth A*. 2020;971:164135. http://dx.doi.org/10.1016/j.nima.2020.164135.
7. Xiu D, Karniadakis GE. The Wiener-Askey polynomial chaos for stochastic differential equations. *SIAM J Sci Comput*. 2002;24(2):619-644.
8. Hale N, Trefethen LN. New quadrature formulas from conformal maps. *SIAM J Numer Anal*. 2008;46(2):930-948.
9. TrefethenLN. *Approximation Theory and Approximation Practice*. Vol 128. Philadelphia, PA: SIAM; 2013.
10. JantschP, Webster C. *Sparse Grid Quadrature Rules Based on Conformal Mappings*. Cham, Switzerland: Springer; 2018:117-134.
11. GeorgN, Loukrezis D, Römer U, Schöps S. Enhanced adaptive surrogate models with applications in uncertainty quantification for nanoplasmonics. *Int J Uncertainty Quantif*. 2020;10(2). https://doi.org/10.1615/Int.J.UncertaintyQuantification.2020031727.
12. Tsilifis P, Ghanem RG. Reduced Wiener chaos representation of random fields via basis adaptation and projection. *J Comput Phys*. 2017;341:102-120.
13. Papaioannou I, Ehre M, Straub D. PLS-based adaptation for efficient PCE representation in high dimensions. *J Comput Phys*. 2019;387:186-204.
14. Jin JM. *The Finite Element Method in Electromagnetics*. Hoboken, NJ: John Wiley & Sons; 2015.
15. MonkP. *Finite Element Methods for Maxwell's Equations*. Oxford, UK: Oxford University Press; 2003.
16. Nédélec JC. Mixed finite elements in R^3. *Numer Math*. 1980;35(3):315-341. https://doi.org/10.1007/BF01396415.
17. Lebrun R, Dutfoy A. Do Rosenblatt and Nataf isoprobabilistic transformations really differ? *Probab Eng Mech*. 2009;24(4):577-584.
18. HiptmairR, Scarabosio L, Schillings C, Schwab C. Large deformation shape uncertainty quantification in acoustic scattering. *Adv Comput Math*. 2018;44:1475-1518.
19. Aylwin R, Jerez-Hanckes C, Schwab C, Zech J. Domain uncertainty quantification in computational electromagnetics. 2019.
20. Wiener N. The homogeneous chaos. *Am J Math*. 1938;60(4):897-936.
21. Soize C, Ghanem R. Physical systems with random uncertainties: chaos representations with arbitrary probability measure. *SIAM J Sci Comput*. 2004;26(2):395-410.
22. Ernst OG, Mugler A, Starkloff HJ, Ullmann E. On the convergence of generalized polynomial chaos expansions. *ESAIM: Mathematical Modelling and Numerical Analysis*. 2012;46(2):317-339.
23. Xiu D. *Numerical Methods for Stochastic Computations: A Spectral Method Approach*. Princeton, NJ: Princeton University Press; 2010.
24. BoydJP. *Chebyshev and Fourier Spectral Methods*. 2nd ed. New York, NY: Dover Publications; 2001.
25. Babuška I, Nobile F, Tempone R. A stochastic collocation method for elliptic partial differential equations with random input data. *SIAM J. Numer. Anal*. 2007;45(3):1005-1034.
26. Hale N. On the Use of Conformal Maps to Speed Up Numerical Computations [PhD thesis]. Oxford University; 2009.
27. Sobol IM. Global sensitivity indices for nonlinear mathematical models and their Monte Carlo estimates. *Math. Comput. Simul*. 2001;55(1):271-280. https://doi.org/10.1016/S0378-4754(00)00270-6.

28. Feinberg J, Langtangen HP. Chaospy: an open source tool for designing methods of uncertainty quantification. *J Comput Sci*. 2015;11:46-57.
29. CST AG. Optical applications with CST microwave studio. https://www.cst.com/content/events/downloads/euc2012/talk_5-3-1_cst_euc_2012.pdf. 2012. Accessed March 12, 2018.
30. Alnæs M, Blechta J, Hake J, et al. The FEniCS project version 1.5. *Arch Numer Softw*. 2015;3(100):9-23.
31. Braibant V, Fleury C. Shape optimal design using B-splines. *Comput Methods Appl Mech Eng*. 1984;44(3):247-267. https://doi.org/10.1016/0045-7825(84)90132-4.
32. Schmitt N, Georg N, Brière G, et al. Optimization and uncertainty quantification of gradient index metasurfaces. *Opt Mater Express*. 2019;9(2):892-910. https://doi.org/10.1364/OME.9.000892.
33. Nobile F, Tempone R. Analysis and implementation issues for the numerical approximation of parabolic equations with random coefficients. *Int J Numer Meth Eng*. 2009;80(6-7):979-1006.

How to cite this article: Georg N, Römer U. Conformally mapped polynomial chaos expansions for Maxwell's source problem with random input data. *Int J Numer Model El*. 2020;33:e2776. https://doi.org/10.1002/jnm.2776